Ⓔ

Surface Deformation of North-Central Oklahoma Related to the 2016 M_w 5.8 Pawnee Earthquake from SAR Interferometry Time Series

by Eric J. Fielding, Simran S. Sangha, David P. S. Bekaert, Sergey V. Samsonov, and Jefferson C. Chang

ABSTRACT

The 3 September 2016 M_w 5.8 Pawnee earthquake shook a large area of north-central Oklahoma and was the largest instrumentally recorded earthquake in the state. We processed Synthetic Aperture Radar (SAR) from the Copernicus Sentinel-1A and Sentinel-1B and Canadian RADARSAT-2 satellites with interferometric SAR analysis for the area of north-central Oklahoma that surrounds Pawnee. The interferograms do not show phase discontinuities that would indicate surface ruptures during the earthquake. Individual interferograms have substantial atmospheric noise caused by variations in radar propagation delays due to tropospheric water vapor, so we performed a time-series analysis of the Sentinel-1 stack to obtain a more accurate estimate of the ground deformation in the coseismic time interval and the time variation of deformation before and after the earthquake. The time-series fit for a step function at the time of the Pawnee shows about 3 cm peak-to-peak amplitude of the coseismic surface deformation in the radar line of sight with a spatial pattern that is consistent with fault slip on a plane trending east-southeast. This fault, which we call the Sooner Lake fault, is parallel to the west-northwest nodal plane of the U.S. Geological Survey National Earthquake Information Center moment tensor solution. We model the fault plane by fitting hypoDD-relocated aftershocks aligned in the same trend. Our preferred slip model on this assumed fault plane, allowing only strike-slip motion, has no slip shallower than 2.3 km depth, an area of moderate slip extending 7 km along strike between 2.3 and 4.5 km depth (which could be due to aftershocks and afterslip), and larger slip between 4.5 and 14 km depth extending about 12 km along strike. The large slip below the 4.5 km depth of our relocated hypocenter indicates that the coseismic rupture propagated down-dip. The time-series results do not show significant deformation before or after the earthquake above the high atmospheric noise level within about 40 km of the earthquake rupture.

probability density functions for the smoothing factors of the alternative slip model, and outputs of the Generic Interferometric Synthetic Aperture Radar (InSAR) Analysis Toolbox (GIAnT) time-series analysis.

INTRODUCTION

The state of Oklahoma has suffered a drastic increase in the number of earthquakes since 2009, mainly rupturing subsurface strike-slip faults (Keranen *et al.*, 2014; McNamara *et al.*, 2015). During 2016, there were three earthquakes in Oklahoma with magnitude $M_w \geq 5.0$, including a 5.1 near Fairview in February (Yeck *et al.*, 2016), a 5.8 near Pawnee in September (Yeck *et al.*, 2017), and a 5.0 near Cushing in November (Fig. 1). A previous M_w 5.7 earthquake and two M_w 5.0-related shocks struck near Prague, Oklahoma, in 2011 (Keranen *et al.*, 2013; Sumy *et al.*, 2014). All recent M_w 5+ earthquakes (moment magnitudes here from the U.S. Geological Survey [USGS] National Earthquake Information Center [NEIC]) and almost all of the smaller earthquakes have occurred in the parts of Oklahoma where the sedimentary rocks are present but less than 4 km thick over crystalline basement that is probably composed of fractured igneous or metamorphic rocks (Shah and Keller, 2016).

The 3 September 2016 M_w 5.8 Pawnee earthquake shook a large area of north-central Oklahoma and is the largest instrumentally recorded earthquake in the state to date (Yeck *et al.*, 2017). The increased seismic activity in Oklahoma has been interpreted by many authors to be due to increase in wastewater injection related to petroleum operations (Keranen *et al.*, 2014; McNamara *et al.*, 2015; Yeck *et al.*, 2016), but we do not address the triggering in this brief report. Here, we focus on estimating the location and distribution of slip during the Pawnee earthquake. The mainshock epicenter was located 14 km northwest of the city of Pawnee (Yeck *et al.*, 2017), county seat of Pawnee County, and a number of houses and buildings in and around Pawnee suffered nonstructural
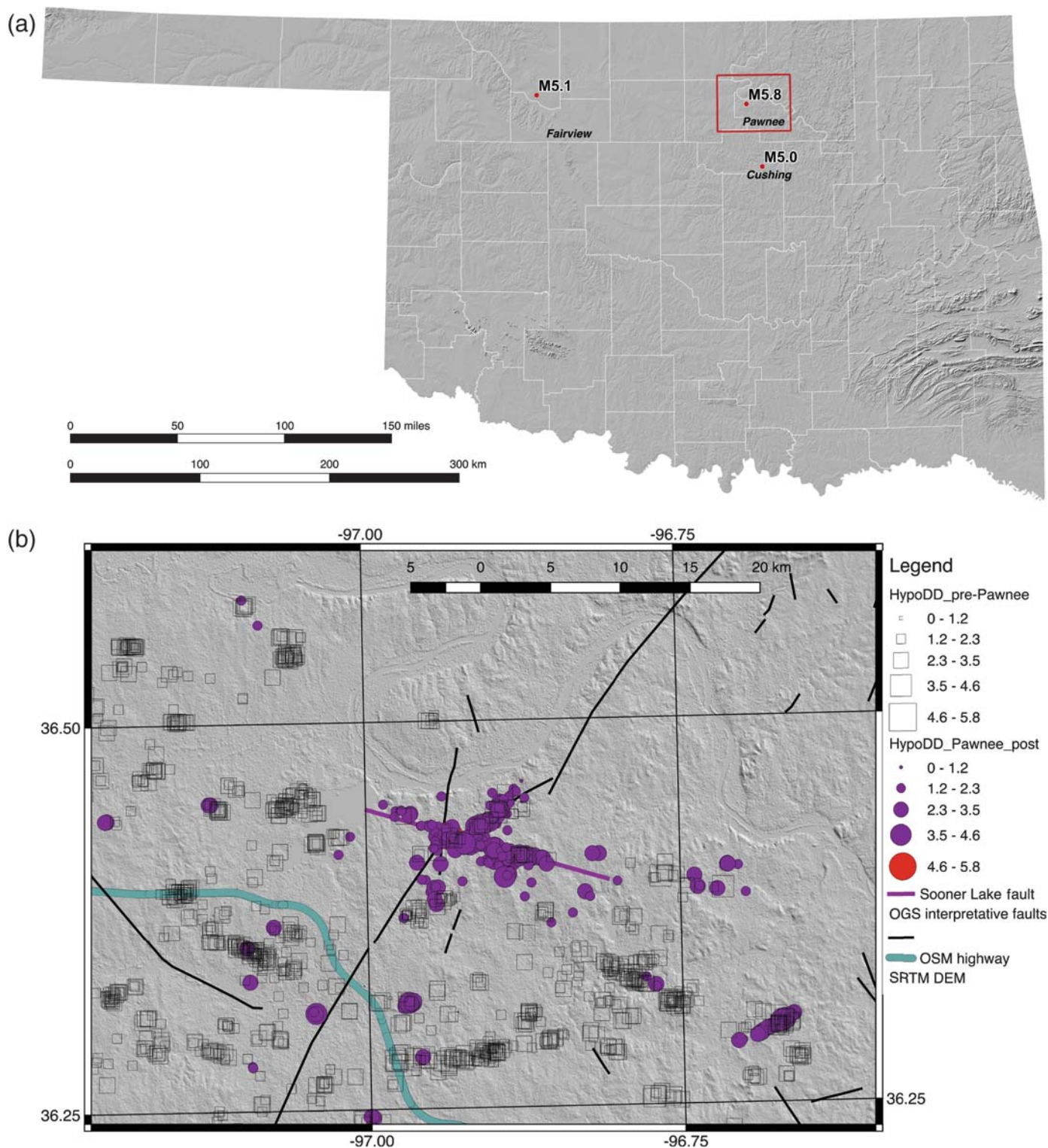
▲ **Figure 1.** (a) Location map of the 2016 M_w 5.1 Fairview, 2016 M_w 5.8 Pawnee, and 2016 M_w 5.0 Cushing earthquakes (circles) in Oklahoma with shaded relief lighting from northwest. Box shows location of Figure 2. (b) Seismicity in the Pawnee area since December 2012, relocated with hypoDD, over a shaded relief map from Shuttle Radar Topography Mission (SRTM) v.3 elevation model. Open squares show events before Pawnee earthquake on 3 September 2016; circles filled with purple show the earthquakes after the Pawnee earthquake through 14 November 2016. Shaded relief lighting is from northeast. Black lines show interpretive faults (Marsh and Holland, 2016). Magenta line is estimated location of Sooner Lake fault. The cyan line is a major highway from Open Street Map.
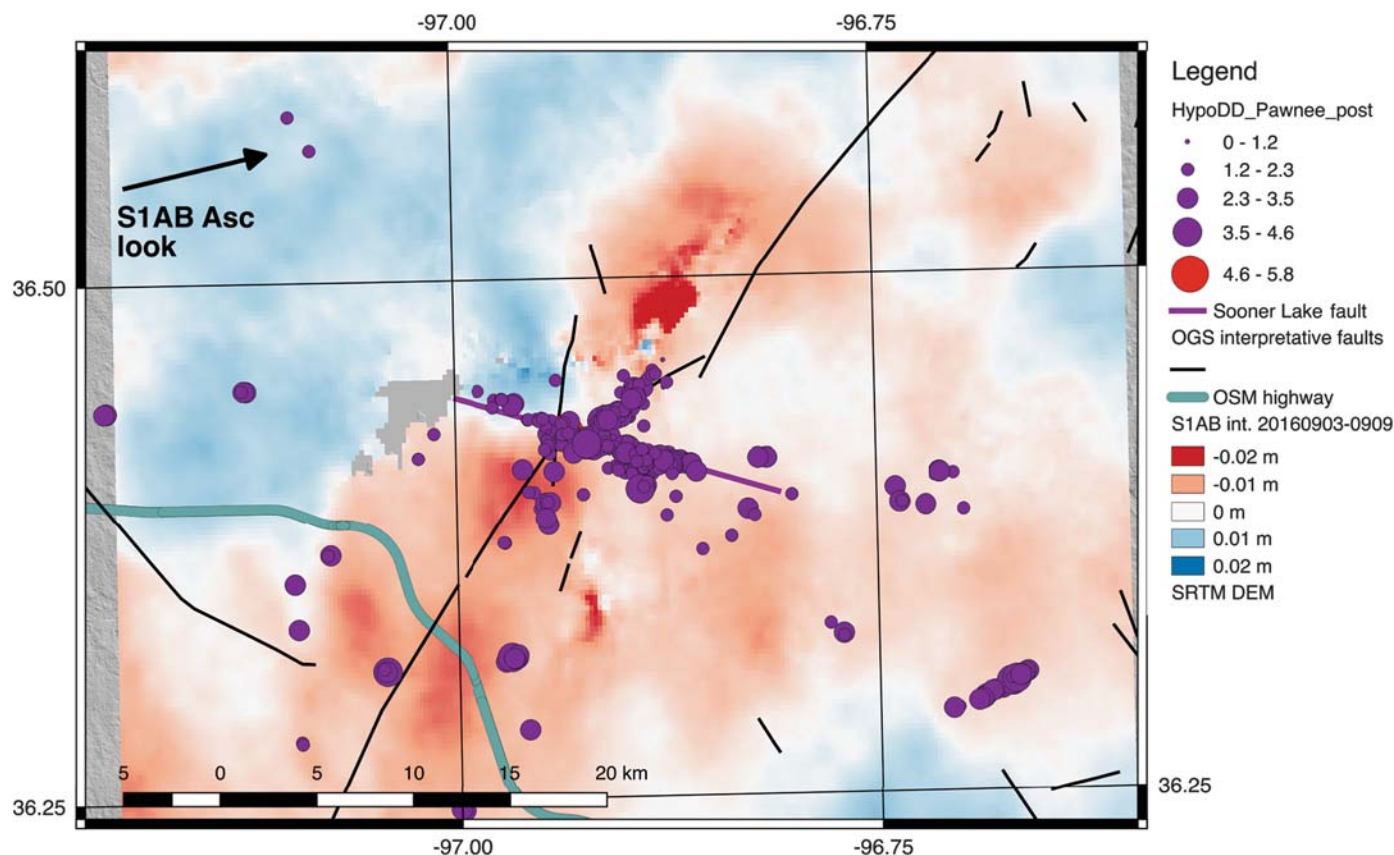
▲ **Figure 2.** Sentinel-1A/1B 6-day coseismic interferogram (3–9 September 2016) in the Pawnee area converted to line-of-sight (LoS) change with overlay of earthquakes relocated with hypoDD. Purple circles show aftershock locations, and a red circle shows the main-shock epicenter (mostly hidden). Arrow shows direction of LoS from satellite to ground. Positive deformation is toward the satellite, either up or west. Black lines show faults from Oklahoma Geological Survey fault database (Marsh and Holland, 2016). The thick cyan line is a major highway. The magenta line is our model fault location. Background is SRTM shaded relief.

damage, including failed facades and chimneys (Clayton *et al.*, 2016). Most of the aftershocks formed a linear trend toward the south-southeast from the mainshock epicenter (Fig. 2), which is consistent with one of the optimal fault orientations estimated from focal mechanisms in the area south of Pawnee (Holland, 2013).

FAULT GEOMETRY AND SEISMICITY

We relocated 2172 events of $M_w \geq 1$ in the Oklahoma Geological Survey (OGS) earthquake catalog within ∼50 km of the Sooner Lake fault using hypoDD (Waldhauser and Ellsworth, 2000). We used phase picks from the local network operated by the OGS, along with USGS, Incorporated Research Institutions for Seismology, and other regional networks, operating from 12 December 2012 to 6 January 2017. The 1D velocity model (Table 1) was determined using VELEST (Kissling *et al.*, 1994) and an assumed V_P/V_S ratio of 1.73. Although the OGS catalog has a magnitude of completeness (M_c) of 2.4, we used analyzed events of M_w 1 and greater to better delineate the seismogenic faults in the area. We plot the relocated events since December 2012 over a shaded relief map in Figure 1b, and the

relocated catalog is available in Ⓔ Table S1 (available in the electronic supplement to this article). Both the seismicity before the 3 September 2016 Pawnee earthquake and after that time is limited to areas to the west and south of the Arkansas River (the large river just north of Pawnee that forms the county boundary in this area). This could be due to a change in the basement rock type or history (Shah and Keller, 2016). The aftershocks of the

Table 1
Velocity Model Used for Pawnee Area hypoDD Analysis

Top (km)	Velocity (km/s)*
0	2.7
0.3	2.95
1	4.15
1.5	5.8
8	6.27
21	6.41
42	7.9
50	8.15

*P-wave velocity, with assumed V_P/V_S ratio of 1.73.

Pawnee earthquake largely fall along a line striking east-southeast from the M_w 5.8 epicenter (Fig. 1b). We manually defined a line through the aftershock alignment to use as our model fault location (see Fig. 1b). This fault was named the Sooner Lake fault by the OGS because it passes under the Sooner Lake near its western end and is the same fault referred to as the Pawnee fault by Yeck *et al.* (2017).

The OGS has compiled a database of known faults in the state from published sources (Marsh and Holland, 2016). Most of the mapped faults are within the sedimentary section because they have been mapped on seismic reflection profiles by the petroleum industry (Marsh and Holland, 2016; Shah and Keller, 2016). The OGS fault database includes a comprehensive set of all mapped faults, including many duplications, and an interpretative set of significant faults based on the comprehensive set. We plotted the interpretive faults in Figure 1b. The main faults in the area of the Pawnee earthquake strike northeast or north, so the main rupture of the Pawnee earthquake, which we interpret as being on the Sooner Lake fault, is not on one of these previously mapped faults. Some of the foreshocks and aftershocks do align with the northeast-striking Labette fault (Fig. 1b). There were a few events at several locations along the newly interpreted Sooner Lake fault before the Pawnee mainshock, but the seismicity along that line is not noticeably different from the other seismicity to the west and south.

GEODETIC DATA

To measure the surface deformation in the Pawnee area before, during, and after the M_w 5.8 earthquake, we analyzed Synthetic Aperture Radar (SAR) data from two satellite systems: the Copernicus Sentinel-1A and Sentinel-1B satellites operated by the European Space Agency, and the MacDonald, Dettwiler and Associates Ltd. RADARSAT-2 satellite. We performed interferometric SAR (InSAR) analysis for the area of north-central Oklahoma that surrounds Pawnee. We processed multiple interferograms to examine and mitigate noise sources. An overview of the used SAR scenes and formed interferograms are respectively summarized in Table 2 and Ⓔ Table S2. The digital elevation model (DEM) from the Shuttle Radar Topography Mission (SRTM) v.3 (Kobrick and Crippen, 2013) at 1-arcsec spacing (see Data and Resources) was used to remove topographic phase from the interferograms.

We processed 30 Sentinel-1 interferometric wide-swath scenes acquired on ascending track 034 (satellite moving north and looking east) between 23 July 2015 through 26 November 2016. In total, 22 scenes were acquired before the Pawnee earthquake and 8 scenes after the earthquake in the data we analyzed. The typical acquisition repeat intervals for our dataset are 12 and 24 days, except for a 6-day interval (acquisitions on 3 and 9 September 2016) that includes the earthquake (Fig. 2). In total, 63 Sentinel-1 interferograms were formed using the InSAR Scientific Computing Environment (ISCE; Rosen *et al.*, 2012) software. We performed averaging of 33 pixels in across-track direction (range) and 11 pixels along track (azimuth) to reduce noise prior to phase unwrapping

Table 2			
Synthetic Aperture Radar (SAR) Scenes Analyzed			
Sensor	**Track/Pass**	**Date (yyyy/mm/dd)**	**SAR Timing**
S1A	34/Asc.	2015/07/23	Preseismic
S1A	34/Asc.	2015/08/16	Preseismic
S1A	34/Asc.	2015/08/28	Preseismic
S1A	34/Asc.	2015/09/09	Preseismic
S1A	34/Asc.	2015/09/21	Preseismic
S1A	34/Asc.	2015/10/03	Preseismic
S1A	34/Asc.	2015/10/27	Preseismic
S1A	34/Asc.	2015/12/26	Preseismic
S1A	34/Asc.	2016/01/31	Preseismic
S1A	34/Asc.	2016/02/24	Preseismic
S1A	34/Asc.	2016/04/12	Preseismic
S1A	34/Asc.	2016/04/24	Preseismic
S1A	34/Asc.	2016/05/06	Preseismic
S1A	34/Asc.	2016/05/18	Preseismic
S1A	34/Asc.	2016/05/30	Preseismic
S1A	34/Asc.	2016/06/11	Preseismic
S1A	34/Asc.	2016/07/05	Preseismic
RSAT2	2/Des.	2016/07/10	Preseismic
S1A	34/Asc.	2016/07/17	Preseismic
S1A	34/Asc.	2016/07/29	Preseismic
S1A	34/Asc.	2016/08/10	Preseismic
S1A	34/Asc.	2016/08/22	Preseismic
RSAT2	1/Asc.	2016/08/23	Preseismic
S1A	34/Asc.	2016/09/03	Preseismic
S1B	34/Asc.	2016/09/09	Postseismic
S1A	34/Asc.	2016/09/15	Postseismic
RSAT2	1/Asc.	2016/09/16	Postseismic
RSAT2	2/Des.	2016/09/20	Postseismic
S1A	34/Asc.	2016/09/27	Postseismic
S1A	34/Asc.	2016/10/09	Postseismic
RSAT2	1/Asc.	2016/10/10	Postseismic
S1A	34/Asc.	2016/10/21	Postseismic
S1A	34/Asc.	2016/11/02	Postseismic
RSAT2	1/Asc.	2016/11/03	Postseismic
S1A	34/Asc.	2016/11/14	Postseismic
S1A	34/Asc.	2016/11/26	Postseismic
RSAT2	1/Asc.	2016/11/27	Postseismic
S1A, Sentinel-1A; S1B, Sentinel-1B; RSAT2, RADARSAT-2; Asc., ascending track; Des., descending track.			

with Statistical-cost, Network-flow Algorithm for Phase Unwrapping (SNAPHU) program (Chen and Zebker, 2002), resulting in an effective interferogram resolution of about 150 m in both directions. The Sentinel-1 interferograms were geocoded at 3-arcsec (~90 m spacing).

We processed five ascending and two descending RADARSAT-2 scenes using GAMMA software (Wegmuller and Werner, 1997). The ascending RADARSAT-2 strip-map

mode data (Extra Fine-XF0W3-HH, coverage 125 × 125 km, pixel spacing 2.6 × 2.9 m, incidence angle 41°), acquired every 24 days between 23 August 2016 and 27 November 2016, formed in total 10 interferograms over the Pawnee area. Figure 3a shows the 96-day RADARSAT-2 interferogram from 23 August to 27 November 2016 (perpendicular baseline 282 m). The 24-day pair has much worse atmospheric effects, so we did not use it in our slip modeling. The RADARSAT-2 ascending and Sentinel-1 ascending tracks have similar radar imaging geometries. We additionally processed one descending track interferogram (satellite moving south and looking west) from two RADARSAT-2 scenes acquired in the same strip-map mode on 10 July and 20 September 2016 (perpendicular baseline 22 m), with a 72-day time interval (Fig. 3b). The coverage of the descending track is not as complete as the ascending tracks due to the satellite acquisition ending, and the InSAR coherence is lower (incoherent noise level is higher), due to the longer time interval, but it provides helpful data in a different line-of-sight direction. The RADARSAT-2 interferograms were processed with 8 pixels averaged in range and 10 pixels averaged in azimuth to give roughly 30 m pixels in the interferogram processing. The topographic phase was computed from the ∼30−m resolution SRTM DEM (Rabus et al., 2003; Kobrick and Crippen, 2013) and removed from the interferograms. Adaptive filtering (Goldstein and Werner, 1998), phase unwrapping (Costantini, 1998), and geocoding procedures were applied. Because of the low coherence in the RADARSAT interferograms that caused numerous small unwrapping errors, we used a manual method to select patches on the wrong phase ambiguity and applied an unwrapping correction (Jones et al., 2016). After correcting these unwrapping errors, we removed a quadratic ramp from the RADARSAT-2 interferograms and then finally applied a 0.15-km median filter.

The generated interferograms for both Sentinel-1 and RADARSAT-2 are contaminated by tropospheric noise introduced by the spatial and temporal variation of water vapor, pressure, and temperature (Hanssen, 2011; Bekaert et al., 2015). Over Oklahoma, this leads to long-wavelength (> 30−km spatial scale) and turbulent (few kilometers spatial scale) apparent noise signals. Because topographic relief in north-central Oklahoma is small, no large topographically correlated noise is observed. As a test, we applied a tropospheric noise correction to our Sentinel-1 interferograms, based on the Modern-Era Retrospective analysis for Research and Applications (MERRA2) weather model (Bosilovich et al., 2015) to reduce the long-wavelength tropospheric noise effects using the PyAPS program (Jolivet et al., 2014). The correction capability to reduce the turbulent noise was limited because the MERRA2 model is too coarse spatially (∼50−km grid cells) and temporally (6-hr spacing) to capture turbulent effects. We found that the atmospheric corrections did not improve the time-series fits, so we did not use the corrected interferograms in the final slip models. For the single interferograms, we removed a quadratic fit to the phase over a roughly 50 × 50 km subset of the interferograms to mitigate the effects of the residual atmospheric phase on the slip inversion. Because we believe the earthquake slip does not extend

deeper than 15 km, this removal of longer wavelength signals will not interfere with the fault-slip estimates.

The large stack of Sentinel-1 data allowed us to reduce the residual tropospheric noise further through time-series processing. We used the Generic InSAR Analysis Toolbox (GIAnT; Agram et al., 2013) to obtain a more accurate estimate of the ground deformation in the coseismic time interval and the time variation of deformation before and after the earthquake. We did a time-series analysis for the Sentinel-1A/1B scenes from 23 July 2015 through 2 November 2016, fitting the data with a total of five terms, a constant, linear rate, step (Heaviside) function at 3 September 2016, and two seasonal terms. The Sentinel-1 GIAnT time-series analysis included the network-consistent ramp-removal option, which removes linear ramps at the full-scene scale. These results and their associated error estimates are shown in Ⓔ Figures S8–S16. The time-series results for the coseismic step function in the area of the Pawnee earthquake show about 3 cm peak-to-peak amplitude of the coseismic surface deformation in the radar line of sight with a spatial pattern that is similar to the individual interferograms described above but with a smaller level of atmospheric noise (Fig. 4).

The InSAR data, including the time-series fit to the coseismic step function, were cropped to a smaller area around the Pawnee earthquake rupture (−97.2° to −96.6° E and 36.1° to 36.8° N) and downsampled for the fault-slip modeling using a quad-tree approach with varying resampled box sizes (Lohman and Simons, 2005). We used a simple scheme in which the resampled boxes are smallest close to the fault, ∼1.2 km (in longitude direction) × ∼ 1.5 km (in latitude direction) within 10 km, medium at intermediate distances (∼2.4 km× ∼3.0 km between 10 and 20 km distance), and largest at greater distances (∼4.8 km × ∼5.9 more than 20 km away). This keeps higher resampled point density near the fault where it can help resolve the shallow variations in slip and averages over larger areas further away from the fault to reduce noise and effectively downweights the distant samples in the slip inversions, due to their lower spatial density. As mentioned earlier, we also removed quadratic fits to the two RADARSAT-2 interferograms (de-ramped), but not the Sentinel-1 step-function fit, over the cropped area that is roughly 55 × 75 km before doing the resampling. The combination of the larger resampling boxes at larger distances and deramping mitigates the atmospheric noise but does not remove it completely.

GEODETIC SOURCE INVERSION

We use our coseismic InSAR estimates (as described earlier) to constrain a Bayesian inference method with Markov chain Monte Carlo (MCMC) sampling to resolve the fault rupture slip distribution with posterior probability distribution estimates for the smoothing parameters in the strike and dip directions. The Bayesian method is based on Fukuda and Johnson (2008), and our implementation was previously described in Fielding et al. (2013). We use a single planar fault embedded in homogeneous elastic half-space for the earthquake-slip
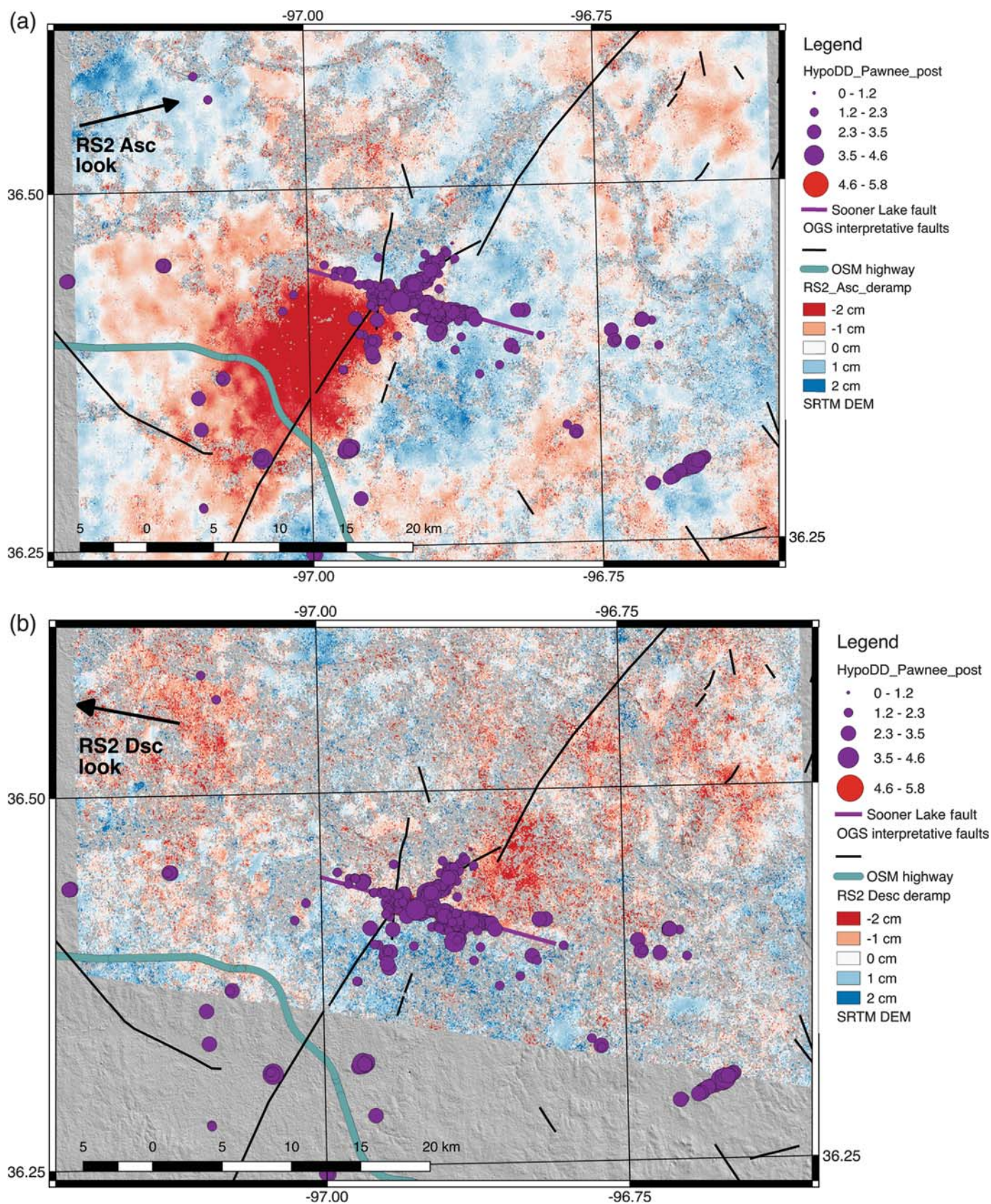
▲ **Figure 3.** RADARSAT-2 coseismic interferograms for same area as Figure 2, both converted to LoS change. Other symbols as in Figure 2. (a) The 96-day interferogram from track with satellite moving north (23 August to 27 November 2016). (b) The 72-day interferogram from track with satellite moving south (10 July to 20 September 2016). Positive deformation is toward the satellite, either up or west.
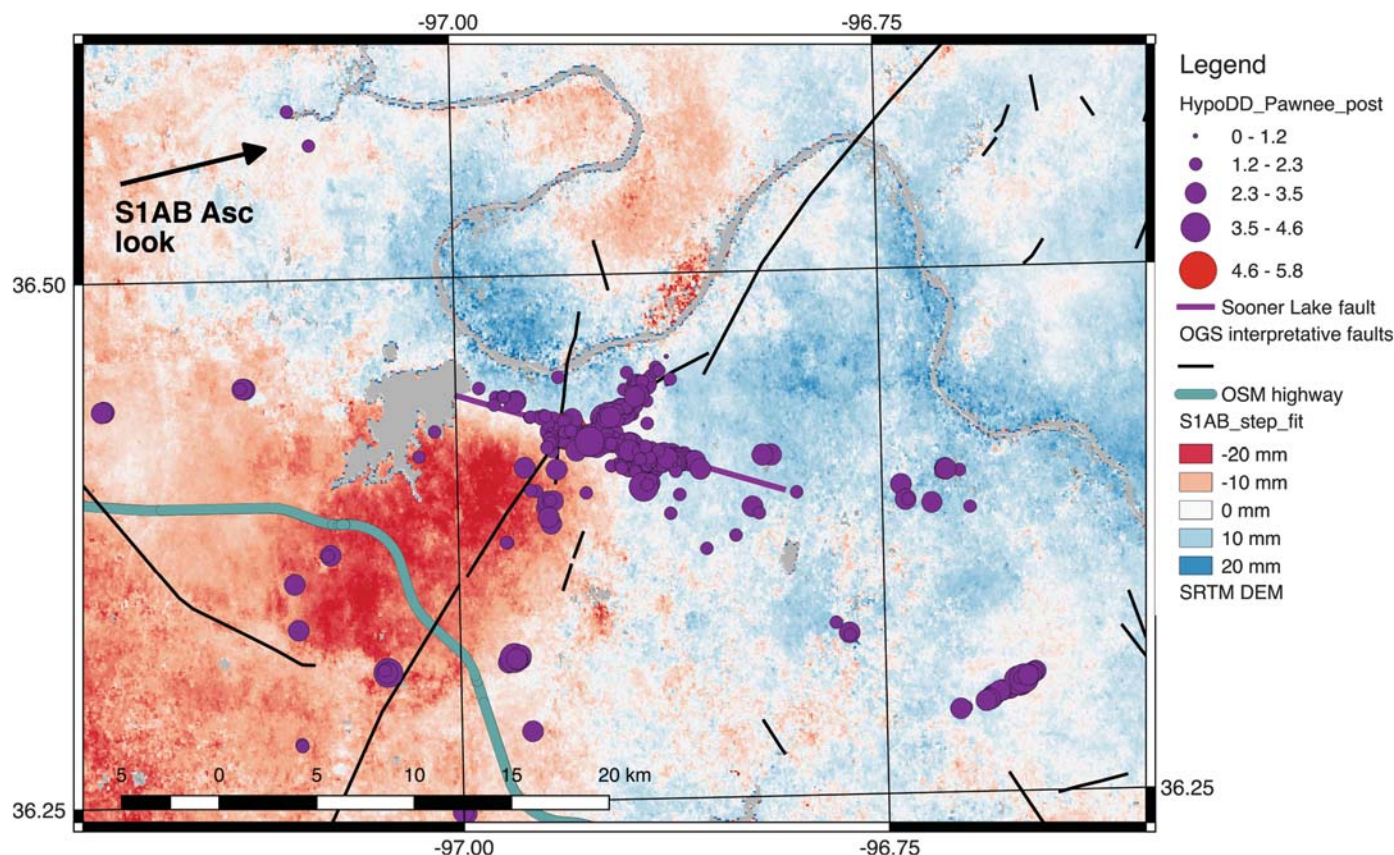
▲ **Figure 4.** Coseismic LoS deformation estimate from Generic interferometric SAR (InSAR) Analysis Toolbox (GIAnT) step function fit to Sentinel-1A/1B time series. Black lines are interpretive faults (Marsh and Holland, 2016). The magenta line is our model fault location (Sooner Lake fault). Positive deformation is toward the satellite, either up or west.

geodetic inversion. We attempted to estimate the model fault location parameters (strike, dip, width, length, and horizontal location) using the MCMC procedure by allowing them to vary, but we found that the results were too unstable to be reliable, due to the high level of residual tropospheric noise in the interferograms compared with the relatively small coseismic deformation signal. Therefore, we fixed the fault location based on the interpreted Sooner Lake fault line described earlier (Figs. 2–4, and 5a). Our model fault dips vertically, has a length of 18 km and a width of 15 km, and is divided into patches that are 1.1 × 1.1 km. We fixed the depth of the top of the model fault to the surface. At each step of the Markov chain sampling of the smoothing parameters, the distribution of slip was estimated using a bounded and weighted least-squares inversion with Laplacian smoothing regularization imposed on the strike-slip (and optionally dip-slip) components of slip on each fault patch. We estimated the relative weighting of the interferogram datasets from the noise variation in a nondeforming area (∼0.27 cm for the Sentinel-1 step function fit; 0.30 cm for the RADARSAT-2 descending track, and 0.72 cm for the RA-DARSAT-2 ascending track). This reduces the contribution of the noisier RADARSAT-2 ascending track data compared with the other two datasets. The slip-inversion algorithm does not explicitly include a positivity constraint, but it does include

a set prior range of allowed values (0–1 m left lateral for the strike-slip component and −1 to +1 m for the dip-slip component). Models with values outside that range are discarded. After each Markov chain step, the weighted root mean square error of the new model fit to the observations was compared with the previous kept fit. The new model is kept if it is better than the previous model or if the exponential of the difference between the previous and current misfits is greater than a random number between zero and one (Fukuda and Johnson, 2008). We introduced an additional constraint after each step to ensure the new model has a geometric moment less than a set value (equivalent to M_w 6.014) and discarded models that were larger. The set of kept solutions after a large number of steps (5000 kept solutions here) forms an estimate of the posterior probability distribution function for the slip smoothing parameters, but it is not a full Bayesian inversion for the slip distribution without regularization such as in the Minson *et al.* (2014) method.

RESULTS

Our relocated earthquake catalog locations are generally shallower by about 2 km on average from Yeck *et al.* (2017). Their relocated events near the epicenter, along the Sooner Lake and
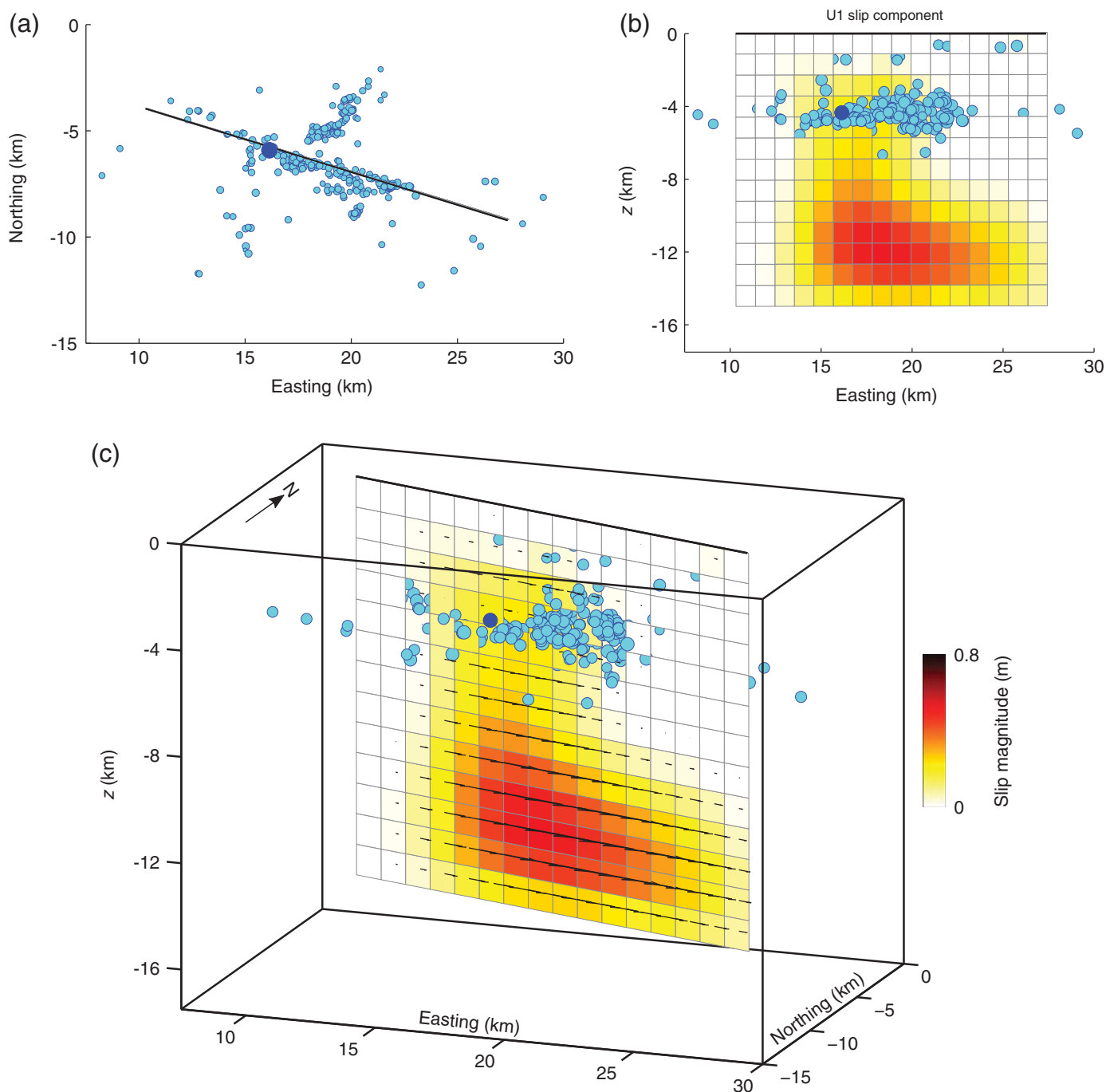
▲ **Figure 5.** Preferred fault-slip model constrained to strike-slip motion with the relocated hypocenters from our hypoDD analysis of the Pawnee aftershocks (cyan circles) and mainshock (large dark blue circle). (a) Map view of model fault location (black line) in local Cartesian coordinate system (kilometers relative to 36.4788° N, −97.1144° E). (b) Slip model distribution on vertical plane, viewed from south. (c) Perspective view of slip distribution from southwest. Arrows show magnitude and direction of motion of southern block relative to northern block.

Labette faults, appear to be shifted to the north by about 300– 500 m when compared with our relocations. These differences could be due to the differing velocity models used in the relocations. Yeck *et al.* (2017) have the top of basement at 1.9 km, whereas we used 1.5 km (Table 1), which is in agreement with several well logs that penetrate basement near the epicenter.

The coseismic interferograms (Figs. 2 and 3) do not show phase discontinuities that would indicate significant surface ruptures during the earthquake, so we conclude that there was no primary surface rupture from the Pawnee earthquake, consistent with the field reports that did not find primary ruptures (e.g., Clayton *et al.*, 2016). Minor secondary cracks and

978 Seismological Research Letters   Volume 88, Number 4   July/August 2017

liquefaction effects reported by the Geotechnical Extreme Events Reconnaissance (GEER) team (Clayton *et al.*, 2016) and others may not be visible in our Sentinel-1 interferograms, due to the relatively coarse spatial resolution (∼150 m) we used in this study. Our preliminary results described here do not show significant deformation before or after the earthquake above the atmospheric noise level (Ⓔ Figs. S8–S16).

Our preferred slip-inversion results come from the MCMC optimization using input data from the step function to the Sentinel-1 time series without atmospheric corrections and the two RADARSAT-2 interferograms, in which we fixed the fault geometry to the hand-picked Sooner Lake fault location, specified a vertical dip, and only allowed strike-slip motion (Fig. 5). We did an approximate estimate of the uncertainty of slip in the preferred model by calculating the standard deviation of the slip on each patch from all 5000 kept models (see Ⓔ Fig. S1). We also ran inversions allowing both strike-slip and dip-slip motion (see Ⓔ Figs. S2–S4), but we do not believe the InSAR data have adequate signal above the noise level to constrain the dip-slip component. Our alternative variable-rake solution has very little change in rake, in part because the Bayesian optimization-found greater smoothing was more likely for the dip-slip component (Ⓔ Figs. S2 and S4). The preferred strike-slip-only model has a smoothing factor of 1.5×10^{-5}, and the seismic moment (M_0) calculated from the geodetic slip model is 1.091×10^{18} N·m (M_w 5.97), using a crustal shear modulus of 30 GPa (the shear modulus around the hypocenter in our velocity model). The geodetic moment is larger than the seismic moment of 6.24×10^{17} N·m or M_w 5.8 (Yeck *et al.*, 2017), which could mean that our model is fitting some residual noise in the data or that the fault geometry is more complex than our model fault. It is also possible that our slip model includes some postseismic afterslip and aftershock slip, but the aftershock total seismic moment is small. The first SAR image acquired after the Pawnee earthquake was on 9 September (Sentinel-1B), 6 days after the mainshock (Table 2). The three downsampled datasets used for the slip inversion, the preferred model predictions, and the residuals are shown in Figure 6. The residual amplitudes are typically around 1–2 cm and are spatially correlated, as expected for tropospheric water vapor variations. The residuals for the three independent InSAR datasets are not correlated with each other, so we believe that the slip model is fitting the coseismic signal well.

In the preferred strike-slip-only model, all of the slip is deeper than 2.3 km beneath the surface, which is consistent with the lack of primary surface ruptures (Fig. 5). Slip greater than 40 cm is deeper than 4.5 km, consistent with the main fault rupture occurring in the crystalline basement beneath the sedimentary section. The shallower slip could be partly due to our regularization function smoothing the slip distribution, but the along-strike extension of the shallower slip is greater than the slip at 6–8 km depth, so it cannot be all due to smoothing. Many of the aftershocks are located between 3 and 5 km depth in this area (Fig. 5), so some of the slip imaged by the InSAR could be due to the aftershocks and possible associated aseismic afterslip.

InSAR measurements of surface displacements are most accurate for estimating the depth of the top of the slip at depth (e.g., Lohman and Simons, 2005; Barnhart and Lohman, 2010; Fielding *et al.*, 2013). The depth of the bottom of the slip is generally less well constrained, especially when the long-wavelength noise level is high, as it is in Oklahoma. In our preferred model, the slip decreases to less than 40 cm at a depth of 14.0 km, but this depends on the smoothing parameter. Our smoothing implementation pulls slip toward zero at the bottom and side edges but not at the top edge. The peak slip amplitude and location, and to a lesser extent the moment, also depend on the smoothing parameter. The centroid of the main slip is at about 10–12 km depth for various values of the smoothing parameter, so that is likely to be robust. Higher levels of smoothing (smaller gamma parameters) make the slip distribution approach a circular patch, but our preferred level of smoothing indicates the along-strike length of slip is roughly the same as the down-dip width of significant slip. A slip inversion without the dataset weighting had a significantly different shape, with the significant slip only extending around 6 km along strike, but had the same vertical extent.

To test whether the deepest slip is required to fit the data, we ran another alternative slip inversion with the model fault extending to only 12 km depth instead of the 15-km model fault width used earlier and the same smoothing toward zero at the bottom (Ⓔ Figs. S5 and S6). The most likely slip model on the narrow fault (Ⓔ Fig. S5) has generally the same shape of significant slip, except that all the deeper slip that formerly extended to 14 km is compressed into the lower 4 km of the fault (8–12 km depth). The estimated M_w 5.95 for this model is almost the same as that of the preferred slip model on the 15 km fault. The misfit of the 12 km fault model is somewhat worse than the 15 km fault model, but the difference of the predicted surface deformation between the two models is less than about 0.2 cm (Ⓔ Fig. S7), within the noise level of the InSAR data. This test shows that the InSAR data are consistent with coseismic slip extending to at least 12 and probably 14 km depth, although we cannot be sure whether all of this apparent signal is due to the earthquake and not partly atmospheric noise.
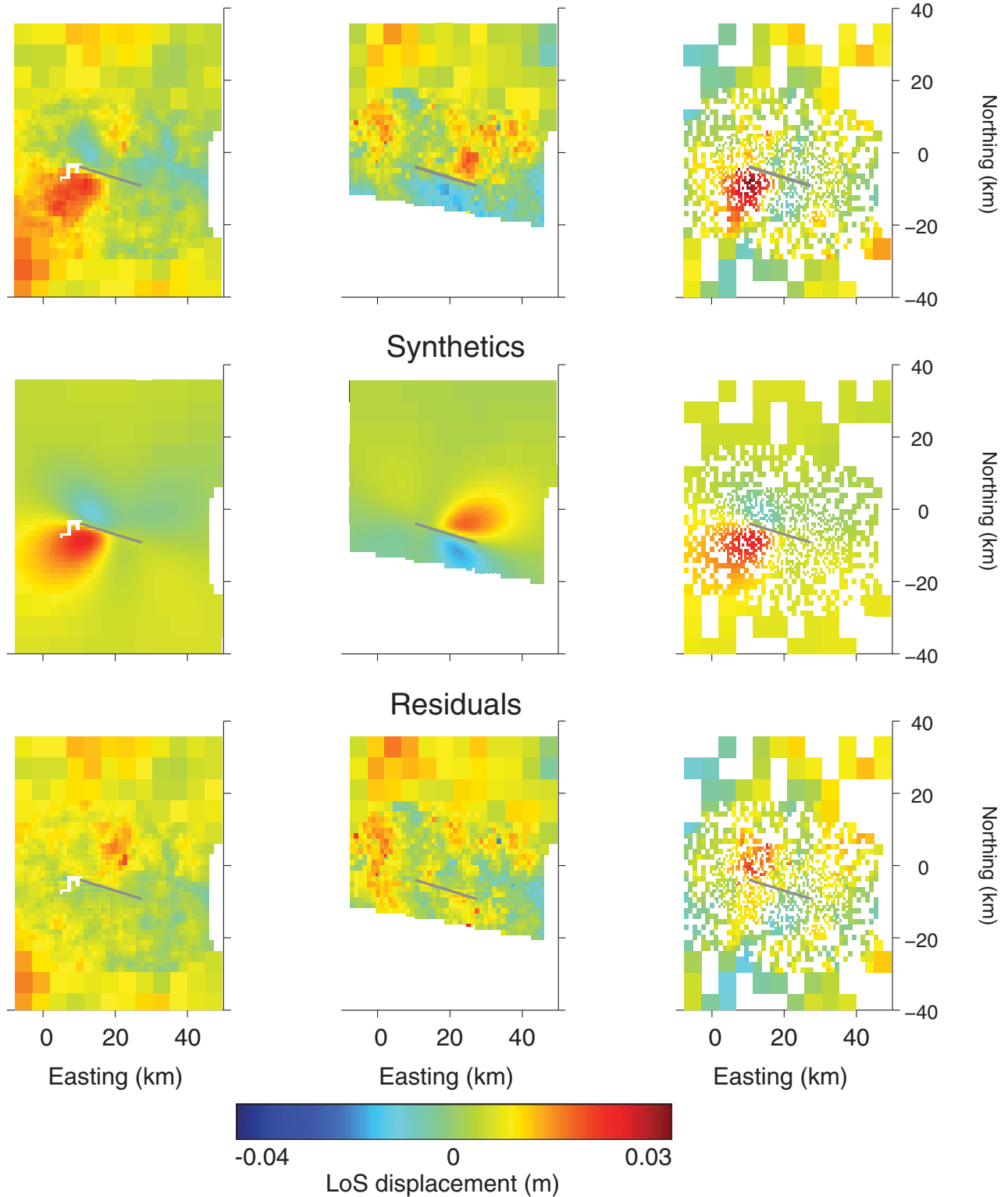
CONCLUSIONS

The 10–11-km centroid depth of the finite-fault slip for the M_w 5.8 Pawnee earthquake that we derive from the InSAR data is more than twice as deep as our relocated hypocenter initiation depth of 4.5 km, so we conclude that the rupture must have propagated down-dip into the basement rocks. Our InSAR-based centroid depth is also consistent with the USGS NEIC W-phase moment tensor centroid depth of 11.5 km. The hypocenter depth would be consistent with the earthquake initiation at a location affected by fluid injection at shallow levels. We hope that more Sentinel-1 data will be acquired to extend the postearthquake analysis and further reduce atmospheric noise. Frequent SAR imaging is helpful to accurately measure the deformation from moderate-sized earthquakes, in addition to

Observed interferograms

Sentinel-1 asc. step-function fit   RSAT-2 desc. 20160710_20160920   RSAT-2 asc. 20160823_20161127

Synthetics

Residuals

Easting (km)   Easting (km)   Easting (km)

Northing (km)

-0.04   0   0.03

LoS displacement (m)

▲ **Figure 6.** Maps of downsampled interferogram data (top row), preferred strike-slip-only model prediction or synthetic (middle row), and residuals (bottom row), all with same color scale. Columns are three InSAR datasets: left is Sentinel-1 time-series coseismic step, middle is RADARSAT-2 descending track, and right is RADARSAT-2 ascending track. Motion in LoS direction on these plots is positive away from the satellite.

providing lower latency for event response. The National Aeronautics and Space Administration–Indian Space Research Organisation (NASA-ISRO) SAR (NISAR) mission planned for launch in 2021 should provide frequent coverage of all land areas.

DATA AND RESOURCES

Generic Mapping Tools (Wessel and Smith, 1998) were used to prepare figures. QGIS (QGIS Development Team, 2016) was used to select items from databases, pick the model fault location, and prepare figures. Generic Interferometric Synthetic Aperture Radar (InSAR) Analysis Toolbox (GIAnT) software (Agram *et al.*, 2013) is available from Caltech under a public license at http://earthdef.caltech.edu (last accessed March 2017). PyAPS—Python based Atmospheric Phase Screen Estimation software is also available from the Caltech EarthDef site. The InSAR Scientific Computing Environment (ISCE) software (Rosen *et al.*, 2012) is available to members of the Western North America Interferometric Synthetic Aperture Radar (WInSAR) Consortium who sign the license agreed with UNAVCO at http://winsar.unavco.org/isce.html (last accessed March 2017). Others may obtain a license for the ISCE software directly from the JPL Office of Technology Transfer http://ott.jpl.nasa.gov/index.php?page=software (last accessed December 2016). Gamma software is a commercial package sold by Gamma RS. Original Copernicus Sentinel-1 data are available at no charge from the Copernicus Sentinels Scientific Data Hub (https://scihub.copernicus.eu/, last accessed March 2017), and are also mirrored at the National Aeronautics and Space Administration (NASA) Alaska Satellite Facility archive center. Shuttle Radar Topography Mission digital elevation models are available for no charge from the NASA–U.S. Geological Survey (USGS) Land Processes Distributed Active Archive Center (https://lpdaac.usgs.gov/, last accessed December 2016). Original RADARSAT-2 data are available for purchase from MacDonald, Dettwiler and Associates Ltd. Oklahoma Geological Survey (OGS) relocated hypocenters over the whole state for 2016 are available from http://wichita.ogs.ou.edu/eq/hypodd/2016/ (last accessed December 2016). The OGS Oklahoma fault database (Marsh and Holland, 2016) Geographic Information Systems (GIS)-compatible files are available from http://www.ou.edu/ogs/data/fault.html (last accessed December 2016). The USGS National Earthquake Information Center moment tensors and hypocenter data are available from http://earthquake.usgs.gov/earthquakes/eventpage/us10006jxs#scientific (last accessed January 2017). ◁

ACKNOWLEDGMENTS

REFERENCES

Agram, P. S., R. Jolivet, B. Riel, Y. N. Lin, M. Simons, E. Hetland, M. P. Doin, and C. Lasserre (2013). New radar interferometric time series analysis toolbox released, *Eos, Trans. AGU* **94,** no. 7, 69–70, doi: 10.1002/2013eo070001.

Barnhart, W. D., and R. B. Lohman (2010). Automated fault model discretization for inversions for coseismic slip distributions, *J. Geophys. Res.* **115,** no. B10, doi: 10.1029/2010jb007545.

Bekaert, D. P. S., R. J. Walters, T. J. Wright, A. J. Hooper, and D. J. Parker (2015). Statistical comparison of InSAR tropospheric correction techniques, *Remote Sens. Environ.* **170,** nos. 40/47, doi: 10.1016/j.rse.2015.08.035.

Bosilovich, M. G., S. Akella, L. Coy, R. Cullather, C. Draper, R. Gelaro, R. Kovach, Q. Liu, A. Molod, P. Norris, *et al.* (2015). MERRA-2: Initial evaluation of the climate, *Technical Report Series on Global Modeling and Data Assimilation*, Vol. **43,** 139 pp.

Chen, C. W., and H. A. Zebker (2002). Phase unwrapping for large SAR interferograms: Statistical segmentation and generalized network models, *IEEE Trans. Geosci. Remote Sens.* **40,** no. 8, 1709–1719.

Clayton, P., G. Zalachoris, E. Rathje, T. Bheemasetti, S. Caballero, X. Yu, and S. Bennett (2016). *The Geotechnical Aspects of the September 3, 2016 M 5.8 Pawnee, Oklahoma Earthquake*, GEER Association, Berkeley, California, doi: 10.18118/G69885.

Costantini, M. (1998). A novel phase unwrapping method based on network programming, *IEEE Trans. Geosci. Remote Sens.* **36,** no. 3, 813–821.

Fielding, E. J., P. R. Lundgren, T. Taymaz, S. Yolsal-Çevikbilen, and S. E. Owen (2013). Fault-slip source models for the 2011 M 7.1 Van earthquake in Turkey from SAR interferometry, pixel offset tracking, GPS, and seismic waveform analysis, *Seismol. Res. Lett.* **84,** no. 4, 579–593, doi: 10.1785/0220120164.

Fukuda, J., and K. M. Johnson (2008). A fully Bayesian inversion for spatial distribution of fault slip with objective smoothing, *Bull. Seismol. Soc. Am.* **98,** no. 3, 1128–1146, doi: 10.1785/0120070194.

Goldstein, R. M., and C. L. Werner (1998). Radar interferogram filtering for geophysical applications, *Geophys. Res. Lett.* **25,** no. 21, 4035–4038.

Hanssen, R. F. (2011). *Radar Interferometry: Data Interpretation and Error Analysis*, Springer, Dordrecht, The Netherlands.

Holland, A. A. (2013). Optimal fault orientations within Oklahoma, *Seismol. Res. Lett.* **84,** no. 5, 876–890, doi: 10.1785/0220120153.

Jolivet, R., P. S. Agram, N. Y. Lin, M. Simons, M.-P. Doin, G. Peltzer, and Z. Li (2014). Improving InSAR geodesy using global atmospheric models, *J. Geophys. Res.* **119,** no. 3, 2324–2341, doi: 10.1002/2013JB010588.

Jones, C. E., K. An, R. G. Blom, J. D. Kent, E. R. Ivins, and D. Bekaert (2016). Anthropogenic and geologic influences on subsidence in the vicinity of New Orleans, Louisiana, *J. Geophys. Res.* **121,** no. 5, 3867–3887, doi: 10.1002/2015JB012636.

Keranen, K. M., H. M. Savage, G. A. Abers, and E. S. Cochran (2013). Potentially induced earthquakes in Oklahoma, USA: Links between wastewater injection and the 2011 M_w 5.7 earthquake sequence, *Geology* **41,** no. 6, 699–702, doi: 10.1130/g34045.1.

Keranen, K. M., M. Weingarten, G. A. Abers, B. A. Bekins, and S. Ge (2014). Sharp increase in central Oklahoma seismicity since 2008 induced by massive wastewater injection, *Science* **345,** 448–451.

Kissling, E., W. L. Ellsworth, D. Eberhart-Phillips, and U. Kradolfer (1994). Initial reference models in local earthquake tomography, *J. Geophys. Res.* **99,** no. B10, 19,635–19,646, doi: 10.1029/93jb03138.

Kobrick, M., and R. Crippen (2013). SRTMGL1: NASA shuttle radar topography Mission Global 1 arc second V003, *NASA EOS-DIS Land Processes DAAC*, U.S. Geological Survey Earth Resources Observation and Science (EROS) Center, Sioux Falls, South Dakota, available at https://lpdaac.usgs.gov/ (last accessed December 2016).

Lohman, R. B., and M. Simons (2005). Some thoughts on the use of InSAR data to constrain models of surface deformation: Noise structure and data downsampling, *Geochem. Geophys. Geosys.* **6,** Q01007, doi: 10.1029/2004GC000841.

Marsh, S., and A. Holland (2016). Comprehensive fault database and interpretive fault map of Oklahoma, *Oklahoma Geol. Surv. Open-File Rept.*, Oklahoma Geological Survey, Norman, Oklahoma, 15 pp.

McNamara, D. E., H. M. Benz, R. B. Herrmann, E. A. Bergman, P. Earle, A. Holland, R. Baldwin, and A. Gassner (2015). Earthquake hypocenters and focal mechanisms in central Oklahoma reveal a complex system of reactivated subsurface strike-slip faulting, *Geophys. Res. Lett.* **42,** no. 8, 2742–2749, doi: 10.1002/2014GL062730.

Minson, S. E., M. Simons, J. L. Beck, F. Ortega, J. Jiang, S. E. Owen, A. W. Moore, A. Inbal, and A. Sladen (2014). Bayesian inversion for finite fault earthquake source models—II: The 2011 great Tohoku-oki, Japan earthquake, *Geophys. J. Int.* **198,** no. 2, 922–940, doi: 10.1093/gji/ggu170.

QGIS Development Team (2016). *QGIS Geographic Information System, Open Source Geospatial Foundation Project*, QGIS Development Team.

Rabus, B., M. Eineder, A. Roth, and R. Bamler (2003). The shuttle radar topography mission—A new class of digital elevation models acquired by spaceborne radar, *ISPRS J. Photogramm. Remote Sens.* **57,** no. 4, 241–262, doi: 10.1016/s0924-2716(02)00124-7.

Rosen, P. A., E. Gurrola, G. F. Sacco, and H. Zebker (2012). The InSAR Scientific Computing Environment, *9th European Conference on Synthetic Aperture Radar*, Nuremberg, Germany, 730–733.

Shah, A. K., and G. R. Keller (2016). Geologic influence on induced seismicity: Constraints from potential field data in Oklahoma, *Geophys. Res. Lett.* **44,** no. 1, 152–161, doi: 10.1002/2016GL071808.

Sumy, D. F., E. S. Cochran, K. M. Keranen, M. Wei, and G. A. Abers (2014). Observations of static Coulomb stress triggering of the November 2011 M 5.7 Oklahoma earthquake sequence, *J. Geophys. Res.* **119,** no. 3, 1904–1923, doi: 10.1002/2013JB010612.

Waldhauser, F., and W. L. Ellsworth (2000). A double-difference earthquake location algorithm: Method and application to the northern Hayward fault, California, *Bull. Seismol. Soc. Am.* **90,** no. 6, 1353–1368, doi: 10.1785/0120000006.

Wegmuller, U., and C. Werner (1997). GAMMA SAR processor and interferometry software, *The 3rd ERS Symposium on Space at the Service of Our Environment*, European Space Agency, Florence, Italy.

Wessel, P., and W. H. F. Smith (1998). New, improved version of the generic mapping tools released, *Eos Trans. AGU* **79,** 579 pp.

Yeck, W. L., G. P. Hayes, D. E. McNamara, J. L. Rubinstein, W. D. Barnhart, P. S. Earle, and H. M. Benz (2017). Oklahoma experiences largest earthquake during ongoing regional wastewater injection hazard mitigation efforts, *Geophys. Res. Lett.* **44,** no. 2, 711–717, doi: 10.1002/2016GL071685.

Yeck, W. L., M. Weingarten, H. M. Benz, D. E. McNamara, E. A. Bergman, R. B. Herrmann, J. L. Rubinstein, and P. S. Earle (2016). Far-field pressurization likely caused one of the largest injection-induced earthquakes by reactivating a large preexisting basement fault structure, *Geophys. Res. Lett.* **43,** no. 19, 10,198–10,207, doi: 10.1002/2016GL070861.

Eric J. Fielding
David P. S. Bekaert
Jet Propulsion Laboratory
California Institute of Technology
4800 Oak Grove Drive
Pasadena, California 91109 U.S.A.
eric.j.fielding@jpl.nasa.gov

Simran S. Sangha
Department of Earth, Planetary, and Space Sciences
University of California, Los Angeles
595 Charles Young Drive East
Box 951567
Los Angeles, California 90095-1567 U.S.A.

Sergey V. Samsonov
Canada Centre for Mapping and Earth Observation
Natural Resources Canada
560 Rochester Street
Ottawa, Ontario
Canada K1A 0E4

Jefferson C. Chang
Oklahoma Geological Survey
University of Oklahoma
100 East Boyd Street, N131
Norman, Oklahoma 73019 U.S.A.